Quantifying Magnetic Domain Correlations in Multilayer Films

Y.U. Idzerda, V. Chakarian, and J.W. Freeland
(Naval Research Laboratory)

ABSTRACT

The vertical correlation of magnetic domains in a Co/Cr/Co magnetic trilayer is statistically quantified as a function of applied magnetic field. These measurements used in conjunction with determinations of the individual layer magnetometry curves identifies the presence of both interlayer anti-ferromagnetic exchange coupling and ferromagnetic dipolar coupling for different regions within the trilayer.

The spin conductance of a magnetic heterostructure is controlled by the relative orientation of the magnetic moment directions of the component layers on a local scale (within a few spin mean-free-paths)[1]. Any meaningful comparison between the measured and calculated spin-conductances for multilayer structures requires a quantitative description of the field dependence of the magnetic domain correlations taken vertically between the layers. The correlation between magnetic domains can be statistically quantified by measuring the magnetic field dependence of the X-ray resonance magnetic scattering (XRMS)[2-5]. XRMS is the angle dependent specular reflectance of circular polarized soft x-rays whose energy is tuned to the absorption energy of a magnetic element present in the multilayer.

The specular scattered intensity of a resonant soft x-ray is a function of the incident angle of the soft x-ray, θ, and the magnetic configuration of the multilayer (which is dependent on the applied magnetic field history). For a single film with magnetic domains large compared to the photon coherence length, the reflected intensity, I(θ,B), is given by

$$I(\theta,B) = \sum_k I_k(\theta)\, x_k(B) \qquad (1a)$$

where k denotes a particular magnetic domain type within the film, I_k the scattered intensity from that domain, and x_k is the fraction of the film in the k^{th} domain type. (Note that $\sum_k x_k(B) = 1$ at any field value.) For a f ilm which has only two possible magnetic domains (left and right), eq. (1a) becomes

$$I(\theta,B) = I^{\rightarrow}(\theta)x^{\rightarrow}(B) + I^{\leftarrow}(\theta)x^{\leftarrow}(B) \qquad (1b)$$

Eq. (1a) can also apply to a multilayer film, but now k denotes a particular configuration of the magnetic moment orientations for each magnetic layer taken vertically along the multilayer. I_k is the scattered intensity from that moment configuration and x_k is the fraction of the multilayer in that particular configuration.[6] Similarly extending eq. (1b) to a magnetic film system consisting of two layers, each with two possible magnetic domain directions, the total scattered intensity becomes

$$I(\theta,B) = I^{\vec{\rightarrow}}x^{\vec{\rightarrow}} + I^{\vec{\leftarrow}}x^{\vec{\leftarrow}} + I^{\overleftarrow{\rightarrow}}x^{\overleftarrow{\rightarrow}} + I^{\overleftarrow{\leftarrow}}x^{\overleftarrow{\leftarrow}} \qquad (2)$$

where $x^{\vec{\rightarrow}}$ and $x^{\overleftarrow{\leftarrow}}$ are the fractions of the film with the magnetic domains of the top and bottom film aligned with each other (correlated) and $x^{\vec{\leftarrow}}$ and $x^{\overleftarrow{\rightarrow}}$ are the fractions of the film anti-aligned to each other (anti-correlated). It is these four magnetic field dependent fractions which will ultimately express the vertical correlation of magnetic domains in the trilayer.

To experimentally realize only these 4 magnetic domain configurations, a magnetic structure with a strong uniaxial magnetic anisotropy is utilized. To accomplish this, a single crystal Co (50Å)/Cr (35Å)/Co (50Å) trilayer is deposited on an epitaxially grown ZnSe(001) substrate. To stabilize the bcc Co structure, a seed layer of 5 Å of bcc Fe is first deposited on the ZnSe. The specular reflected intensity is measured using a Si photodiode

located at an angle 2θ to the incident beam direction (q to the film plane). The 75% circular polarized soft x-ray is tuned to the Co L_3 edge (778 eV), corresponding to the maximum in the Co absorption curve.

To quantify the magnetic domain configuration fractions $x_k(B)$, the applied field dependence of the scattered intensity is measured. But, as indicated in Eq. (1a), the contributions to the total scattered intensity depend separately on the applied magnetic field and on the incidence angle. This latter angular dependence is demonstrated in the top panel of **Figure M-1**, where the log of the specular scattered intensities for negative helicity light and the resulting asymmetry $(I^+ - I^-)/(I^+ + I^-)$ are shown for the sample fully magnetized by an applied field of +120 Oe (I^+) and -120 Oe (I^-). Displayed with these angle dependent reflectance curves are a subset of the field dependent reflected intensity curves recorded at the reported incidence angles (shown in the 8 curves at the bottom of **Figure M-1**). Due to the changing contribution of the scattering intensities $I_k(\theta)$ these curves are markedly different.

The obvious variation in these curves belies a hidden similarity. In eq. (2), the dependence on the applied magnetic field is contained only in the four configuration fractions, $x_k(B)$, whereas the angular dependence is derived solely from the four prefactor terms $I^{\rightarrow}_{\rightarrow}(q)$, $I^{\rightarrow}_{\leftarrow}(q)$, $I^{\leftarrow}_{\rightarrow}(q)$, and $I^{\leftarrow}_{\leftarrow}(q)$ which each remain constant for a fixed incident angle. Therefore, the large variations observed in the field scans taken at different incident angles, results only from a variation of these four multiplicative constants.

Actually only two of these prefactors are unknown. In the top panel of **Figure M-1**, we show the

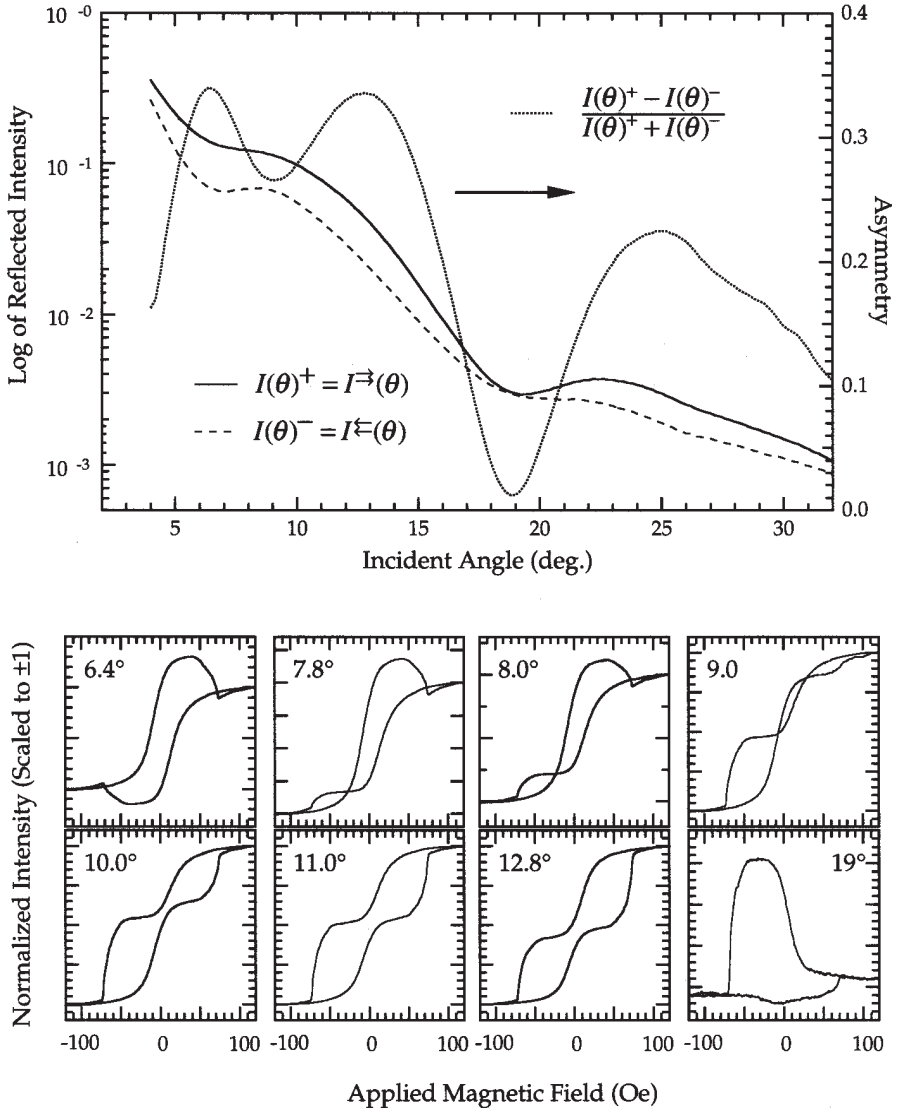

Figure M-1.
(Top Panel) Scattered intensity for circular polarized soft x-rays near the Co L_3 edge (778 eV) for trilayer fully magnetized in either direction. Also shown is the normalized asymmetry.

(Bottom Panel) Eight magnetic field dependent specular intensity spectra acquired at the indicated incidence angle for circular polarized soft x-rays near the Co L_3 edge (778 eV).

experimentally determined values for the angle dependence of the scattered intensity when the film is completely magnetized to saturation in the positive [$x^{\rightarrow}$ =1 and $I^{+}(\theta) = I^{\rightarrow}(\theta)$] or negative [$x^{\leftarrow}$=1 and $I^{-}(\theta) = I^{\leftarrow}(\theta)$] field direction. Utilizing the many field dependent scans, an iterative, least-squares best-fit procedure can be applied to determine the two remaining unknown intensity factors, which are different constants for each angle, and the four configuration fractions, $x^{\rightarrow}$(B), $x^{\leftarrow}$(B), $x^{\rightarrow}$(B), and $x^{\leftarrow}$(B), which must be the same for ALL scans. In this way, the fraction of the film with a particular magnetic domain configuration can be uniquely determined.

The validity of this procedure can be checked by comparing measured magnetometry loops with calculated magnetometry loops derived from the four extracted domain configuration fractions by noting that the moment of the bottom layer, M_{BOTTOM}, is given by

$$M_{BOTTOM} = M_0\left(x_1^{\rightarrow} - x_1^{\leftarrow}\right) \qquad (3)$$

where $x_1^{\rightarrow}$ ($x_1^{\leftarrow}$) is the fraction of the bottom magnetic layer with moment along (opposed to) the applied field direction. This can be rewritten in terms of the four configuration fractions by noting that $x_1^{\rightarrow} = x^{\rightarrow} + x^{\leftarrow}$ and $x_1^{\leftarrow} = x^{\leftarrow} + x^{\leftarrow}$ (and similarly for the top magnetic layer).

In the top panel of **Figure M-2** is shown both the normalized total moment hysteresis curve (measured by vibrating sample magnetometry) as well as the normalized hysteresis curve of just the bottom layer. We have directly measured the hysteretic behavior of the bottom film by measuring the element specific hysteresis curve in absorption of the strongly coupled Fe seed layer used as a template to establish the bcc growth of Co. Superimposed over these curves are the calculated hysteresis loops as determined from the four extracted configuration fractions and eq. (3). The agreement is nearly exact, giving confidence in the extraction of the film fractions.

For spin-conductance applications, it is the relative orientation of the magnetic moments within a domain which gives rise to the resistance variation (aligned for low resistance, anti-aligned for high resistance). Therefore, the correlation function representing the fraction of the film which is aligned, , minus the fraction of the film anti-aligned, , is a more useful quantity to examine. This quantity is plotted in the middle panel of **Figure M-2**.

From **Figure M-2**, it is clear that the Co/Cr/Co film never reaches a fully anti-aligned configuration. The field value where the correlation is most negative corresponds to the peak in the magneto-resistance since it is at this point that the two magnetic layers are most anti-aligned and the trilayer has the highest resistance. This correlation function can be used in conjunction with measured transport curves to extract the coefficient of magnetoresistance[7] or for a detailed comparison with theory. It can also be used to identify and quantify the interlayer coupling mechanisms present in this multilayer.

In the absence of any type of interactions between the magnetic layers, the purely random distribution of magnetic domains will still result in a statistical probability that two vertically offset regions of different magnetic layers within the multilayer are aligned with each other. For two non-interacting independent films, the predicted fraction of the film in a particular configuration, X_{NI}(B), can be calculated as simply the product of the individual domain fractions of each layer (i.e., keeping with the previous notation $x_{NI}^{\rightarrow} = x_1^{\leftarrow} \times x_2^{\rightarrow}$, and similarly for each of the other configurations). Since, as shown in **Figure M-2**, the individual layer fractions can be extracted from either the magnetometry data or the measured two-layer configuration fractions themselves, a correlation function for two non-interacting films can be separately constructed for comparison with the derived correlation function of **Figure M-2**. By comparing the calculated non-interacting films correlation function to the extracted correlation function, we can imply the presence of coupling between the magnetic layers and even ascertain the sign of the coupling.

This comparison is performed in the bottom panel of **Figure M-2** where is shown the bottom film hysteresis curve, the extracted correlation function, and the difference between the extracted correlation function and the calculated correlation function for non-interacting films, each for only the increasing field leg of the hysteresis loop. This difference is just the remainder of the correlation function caused by coupling between the films[8]. As the field is increased, the extracted correlation function is reduced while the bottom film hysteresis loop shows that the bottom film is still near saturation. Since the coupling-derived remainder of the correlation function remains zero, as it must if either film is at saturation, the initial reduction in the extracted correlation function would occur regardless of the presence or absence of any interaction between the films. As the field is increased further, the coupling-derived remainder of the correlation function remains near zero until a significant number of magnetic domains have begun to form in the bottom film. At this point the coupling-derived remainder of the correlation function becomes non-zero and positive, indicating that a significant fraction of the film is interacting and that the magnetic domains are preferentially aligned to those domains directly opposite them in the adjacent layer, probably from dipolar coupling. At higher applied fields, this predominant ferromagnetic interaction is replaced by an anti-

ferromagnetic coupling indicating that the majority of the sample is now dominated by an anti-ferromagnetic interlayer coupling mechanism.

Of the various formulations for describing the magnetic domains with this trilayer system, it is the final coupling-derived remainder of the correlation function associated with interacting films which probes the fundamentally significant behavior of the magnetic films by identifying and quantifying the type and strength of the interlayer coupling mechanisms. ■

This work supported by the office of Naval Research.
V.C. permanent address Etec Systems, Inc. Hayward, CA.
JWF was an NRL/NRC postdoctoral fellow; permanent address Argonne National Laboratory, Argonne, IL.

REFERENCES

[1] P. Bruno and C. Chappert, Phys. Rev. Lett. **67**, 1602 (1991).

[2] K. Namikawa, *et al*., J. Phys. Soc. Jap. **54**, 4099 (1985).

[3] C.-C. Kao, *et al*., Phys. Rev. B (RC) **50**, 9599 (1994).

[4] J. M. Tonnerre, *et al*., , Phys. Rev. Lett. **75**, 740 (1995]=) **75**, 740 (1995).

[5] V. Chakarian, *et al*., J. Magn. Magn. Mater. **165**, 52 (1997).

[6] Here we have ignored intra-domain scattering or scattering from domain walls.

[7] Y. U. Idzerda, *et al*., J. Appl. Phys. **76**, 6525 (1994).

[8] Domain correlations may occur for non-interacting films if growth non-uniformities propogate vertically through a structure, acting as magnetic domain nucleation sites.

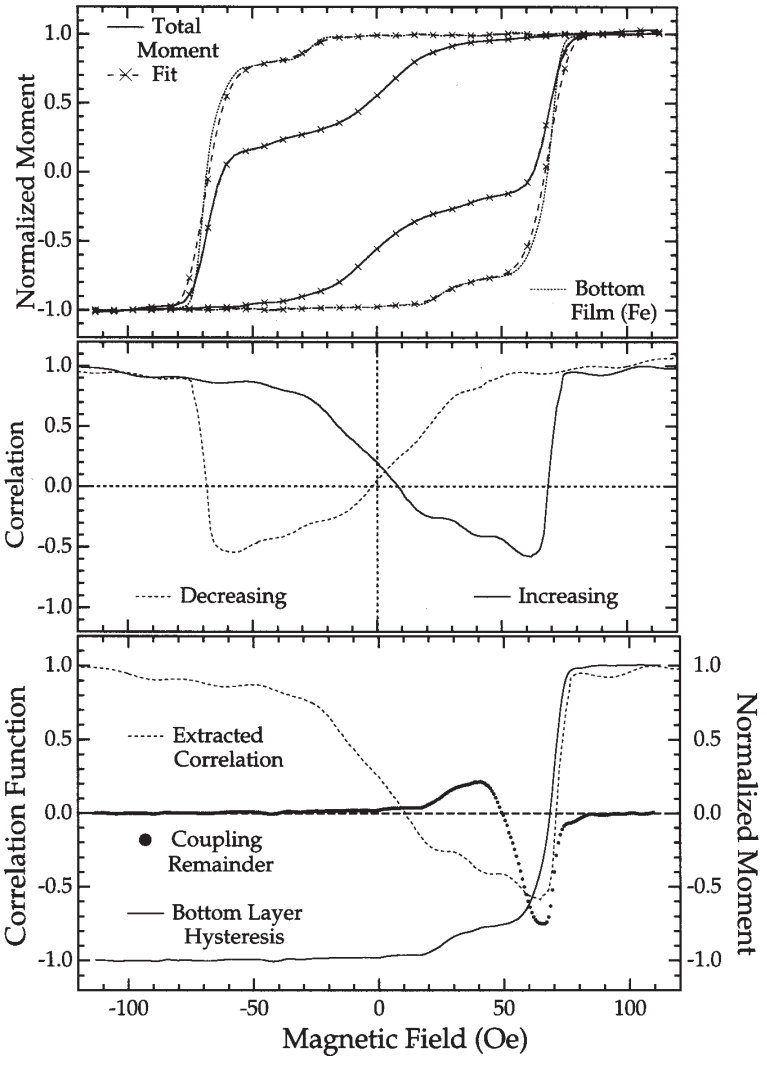

Figure M-2.
(Top Panel) Normalized magnetometry loops for the total moment and only the bottom film (the Fe hysteresis loop). Superimposed is the calculated hysteresis loops from the least-squares best-fit extraction of the configuration fractions (see text).

(Middle Panel) The extracted correlation function (as defined in the text) for increasing (solid) and decreasing (dashed) field.

(Bottom Panel) The bottom layer hysteresis behavior (solid line), the extracted correlation function (dashed line), and the coupling-derived remainder of the correlation function (dots) of the Co/Cr/Co trilayer as a function of increasing field.

Orientational Correlations in Liquid Crystalline Phases Revealed By Polarization-Analyzed Resonant X-Ray Scattering

R. Pindak (Bell Laboratories, Lucent Technologies)
P. Mach (University of Minnesota)
A.-M. Levelut (Univ. Paris-Sud, France)
P. Barois (Centre de Recherche Paul Pascal, U. Bordeaux, France)
C. C. Huang (University of Minnesota),
L. Furenlid (NSLS; current address U. of Arizona))

The existence of a helical symmetry axis is widespread in systems exhibiting liquid crystalline order, especially in systems comprised of chiral molecules. Because these systems usually lack three-dimensional positional order, the helical symmetry axis cannot be observed using conventional x-ray scattering. It is well known that in crystalline systems, resonant x-ray scattering can be used to observe such "hidden" symmetries[1]. In our recent research at NSLS, we demonstrated that polarization-analyzed resonant scattering could also be applied to observe the "hidden" helical symmetry axis in liquid crystals[2]. Since the nature of the helical ordering impacts the electro-optic response of the liquid crystal phase, it is a crucial structural feature to establish.

The liquid crystal systems which we studied are the chiral smectic-C (SmC*) phases. In these phases, the molecules form a stack of fluid-like layers. Within each layer, the molecules, on average, tilt in the same direction. Moreover, the local symmetry environment is consistent with a hindered rotation of the molecules about their long axes resulting in a spontaneous local polarization parallel to the layer plane and perpendicular to the tilt plane (**Figure M-3**). The different SmC* phases are distinguished by different interlayer sequences of changes in the molecular tilt direction. This interlayer orientational order of the molecular tilt varies from the molecules in each layer being tilted in the same direction to the molecules in alternate layers being tilted in opposite directions. Since this interlayer orientational order also applies to the local spontaneous polarization direction, the electro-optic response of the phases varies,

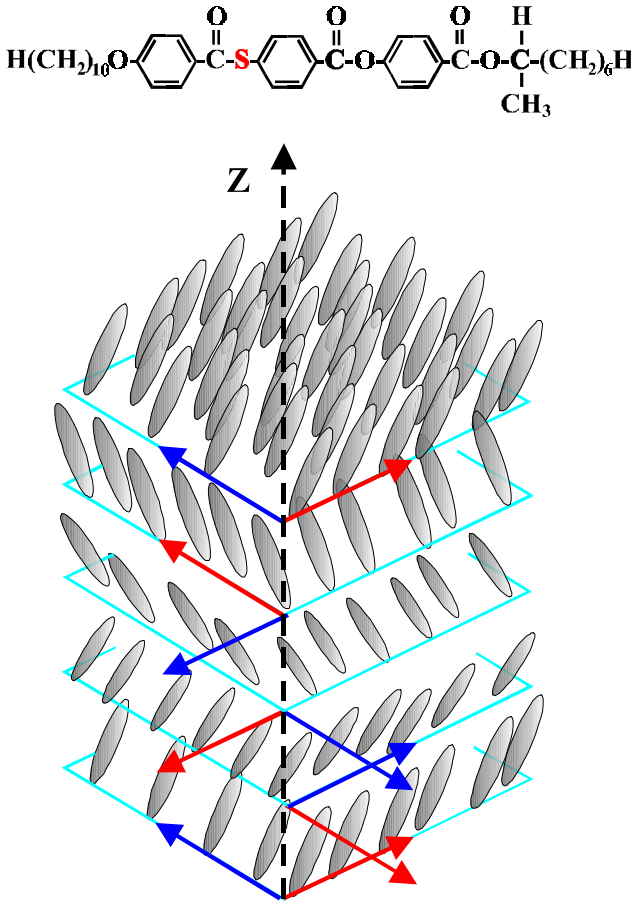

Figure M-3. (Top) Chemical structure of the sulfur-containing thiobenzoate liquid crystal compound studied. (Bottom) Schematic diagram illustrating the structure of the SmC_{FI2}* Phase. The red arrows indicate the direction of the molecular tilt while the blue arrows indicate the direction of the local spontaneous polarization.

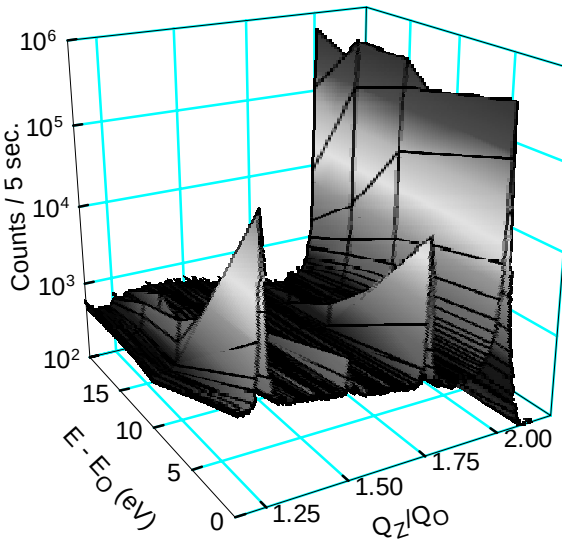

Figure M-4. Diffraction peaks observed in the range $1.2 < Q_z/Q_o < 2.2$ plotted as a function of the energy above the resonance energy E_o. The half and quarter order resonant peaks vanish off-resonance.

phase of the scattered x-rays depend on the orientation of the local environment of the scattering sulfur atom, and therefore, helical modulation of the orientational order can result in diffraction peaks forbidden in convention diffraction. Moreover, the polarization state of the diffracted x-rays can differ from that of the incident x-rays. Dmitrienko calculated the tensorial atomic scattering factor for a crystal with a 4_1 helical symmetry axis[6]. We extended Dmitrienko's analysis to the 4-layer helical structure of the SmC_{FI2}* phase and found that his results also apply; namely, for a s-polarized incident x-ray beam, a structure with a 4_1 helical symmetry axis should produce s-polarized half-order peaks and p-polarized quarter-order peaks.

The existence of quarter and half order resonant peaks for the SmC_{FI2}* phase with the 4-layer helical pitch is shown in **Figure M-4**. Taking the scattering wavevector normal to the layers to be Q_z and the wavevector associated with the layering to be $Q_o=2\pi/d$, the scattered intensity is plotted as a function of both Q_z/Q_o and as a function of the energy departure of the incident x-rays from the resonant energy, E_o. It is evident that when $(E-E_o) > 20$ eV, only the integer order $Q_z/Q_o = 2.0$ peak remains within the range of wavevectors probed.

To measure the polarization state of the scattered x-rays, we used a pyrolytic graphite (PG) analyzing crystal. At the sulfur resonant energy, the 2θ Bragg angle for PG is close to 90° so rotating the analyzing crystal about the

axis of the x-ray beam through the angle, χ_a , will diffract most of the beam if the beam is polarized perpendicular to the PG diffraction plane, but will diffract nearly zero beam if polarized parallel to this plane. The top plot in **Figure M-5** illustrates this for the incident beam. The incident beam was σ-polarized and was polarized perpendicular to the PG diffraction plane when $\chi_a = \pm 90°$ giving maxima in the diffracted intensity. We applied a similar polarization analysis to the resonant peaks in the SmC_{FI2}* phase (lower three plots in **Figure M-5**) by rotating the analyzer crystal about the diffracted beam. For the half order peak, the diffracted beam was σ-polarized, same as the incident beam, giving χ_a maxima at ± 90°. On the other hand, for the two quarter order peaks, the diffracted beam was π-polarized so the maximum in χ_a occurs at 0° as predicted by the tensor analysis for the 4_1 helical symmetry.

In summary, we showed that polarization-analyzed resonant x-ray scattering provides a valuable and unique probe of the orientational correlations that occur in liquid crystalline systems. These orientation correlations can be studied from Angstrom to micron length scales. The observed polarizations agree with a clock-model of the SmC* phases, and unambiguously rule out other proposals made to date for these structures. ■

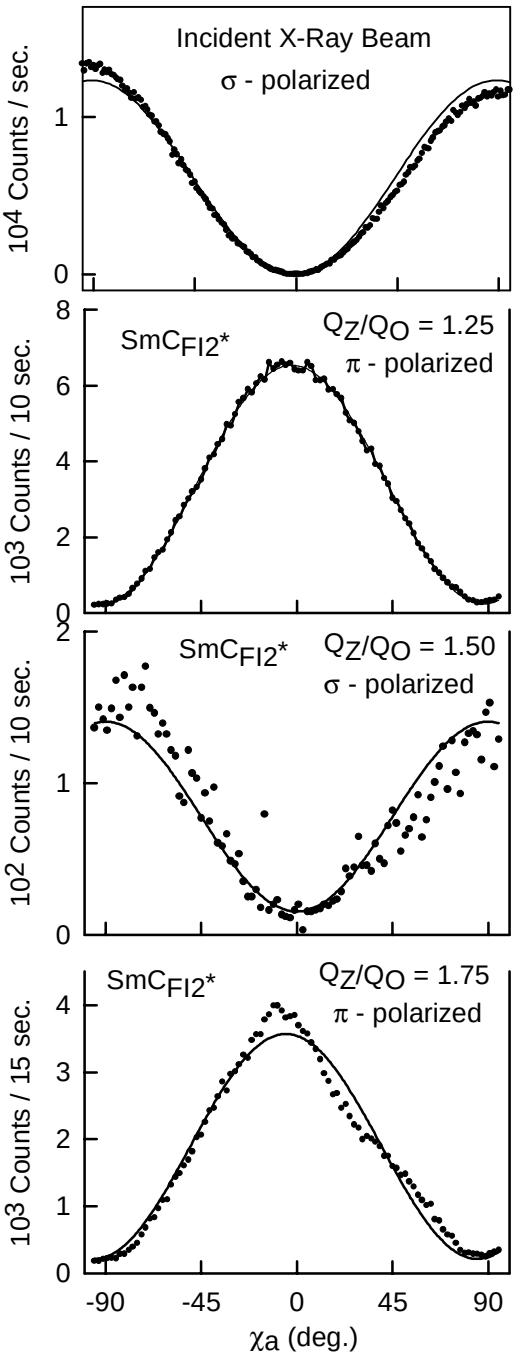

Figure M-5. *Upper Plot* Intensity diffracted by the PG polarization analyzer as it was rotated through an angle, χ_a, around the incident x-ray beam. This scan was taken at an energy where the PG 2θ Bragg angle = 90°. *Lower Three Plots* These plots, taken at the sulfur K-edge energy, show the intensity diffracted by the PG polarization analyzer as it was rotated about the resonant diffracted x-ray beam for the quarter and half order peaks in Figure M-4.

REFERENCES

[1] D. H. Templeton and L. K. Templeton, Acta Cryst. **A42**, 478 (1986); L. K. Templeton and D. H. Templeton, *Acta Cryst.* **A44**, 1045 (1988).

[2] P. Mach, R. Pindak, A.-M. Levelut, P. Barois, H. T. Nguyen, C. C. Huang, and L. Furenlid, *Phys. Rev. Lett.* **81**, 1015 (1998).

[3] H. T. Nguyen, J. C. Rouillon, P. Cluzeau, G. Sigaud, C. Destrade, and N. Isaert, *Liq. Cryst.* **17**, 571 (1994).

[4] M. Cepic and B. Zeks, *Mol. Cryst. Liq. Cryst.* **263**, 61 (1995); V. L. Lorman, *Mol. Cryst. Liq. Cryst*. **262**, 437 (1995); A. Roy and N. Madhusudana, *Europhys. Lett.* **36**, 221 (1996).

[5] A. Fukuda, Y. Takanishi, T. Isozaki, K. Ishikawa, and H. Takezoe, *J. Mater. Chem.* **4**, 997 (1994) and references cited in this review.

[6] V. E. Dmitrienko, *Acta Cryst.* **A39**, 29 (1983).

Surface and Bulk Electronic Structure in Wide Band Gap Nitride Semiconductors

K.E. Smith
(Department of Physics, Boston University)

INTRODUCTION

Wide band gap nitride semiconductors are the focus of intense scientific scrutiny due to their numerous potential applications in optoelectronic and high temperature devices.[1] However, our understanding of the basic physics of these materials lags far behind our ability to make simple electronic devices from them. If wide band gap nitride semiconductors are to achieve their full technological potential then we must have as deep an understanding of their *fundamental* properties as exists for Si and III-V electronic materials. We have begun a program aimed at understanding both the basic electronic structure of a variety of wide band gap nitride semiconductors, and also the electronic structure of metal and non-metal overlayers on these nitrides. We use a unique combination of photon and electron spectroscopies in this effort, and our experiments are primarily performed on NSLS beamlines U4A and X1B.

EXPERIMENTAL TECHNIQUES

Four complimentary spectroscopic probes of electronic structure in solids are utilized in this program: angle resolved photoemission spectroscopy (ARP) and soft x-ray emission spectroscopy (SXE) being the primary tools, and soft x-ray absorption spectroscopy (SXA) and inverse photoemission spectroscopy (IPS) being secondary tools. ARP is a well established technique that allows us to measure the band dispersion of both bulk and surface states in solids. However, the short mean free path of electrons in solids leads to a very high surface sensitivity for ARP, which requires that the surface of the sample under consideration be atomically clean and well ordered. In contrast, as a photon in/photon out spectroscopy, SXE is a bulk probe. SXE measures the element- and site-specific density of states resolved into its orbital angular momentum components. A renaissance in SXE is presently underway due to two factors: i) the combined use of grazing incidence diffraction gratings to disperse the x-ray emission and a wide area x-ray detector to measure the emission, that can be moved under vacuum to remain at the focal point of the gratings for all energies, and ii) the use of high intensity monochromatic synchrotron radiation as the excitation source.[2-4] The former allows energy resolution comparable to that of conventional photoemission to be obtained, while the latter allows the selective excitation of individual core levels in multi-element systems. An added feature of our SXE spectrometer is the ability to be used as a high energy inverse photoemission spectrometer, since the physical process leading to inverse photoemission is similar to that leading to electron-excited SXE.[5, 6]. In a collaboration with Dr. Peter Johnson from BNL Physics, we also have used his dedicated IPS instrument in this program. Finally, we also have used SXA spectroscopy, which gives complimentary information concerning the empty density of states.[7]

RESULTS

Among the highlights of our nitride research program thus far are:

- The first *full* measurement of the bulk valence band dispersion of wurtzite GaN;
- The *definitive* observation and characterization of surface states on GaN(0001);
- The commissioning of a new high resolution x-ray emission spectrometer on X1B, and its use to measure the *elementally resolved* valence band electronic structure in GaN, AlN, $Al_xGa_{1-x}N$, and GaN_xAs_{1-x}
- The direct measurement of shallow core level hybridization in semiconductors;
- The measurement of *elementally resolved* band gap evolution in $Al_xGa_{1-x}N$
- A measurement of the dispersion of conduction band states using inverse photoemission spectroscopy.

i) *Bulk Band Dispersion in GaN*: The full bulk band dispersion of the occupied valence states in n-type wurtzite GaN was measured for the first time.[8, 9] Figure 1 shows a series of photoemission spectra where states along the GM direction in the bulk Brillouin zone are being probed. The rich set of spectra in **Figure M-6** are representative of those measured in other directions, and indicative of the high quality of the surfaces being studied. Since ARP is a surface sensitive technique, the bulk band

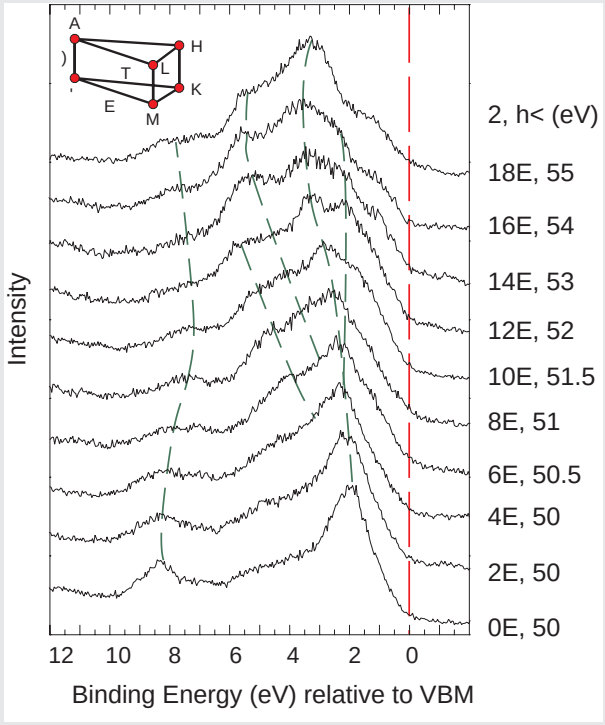

Figure M-6.

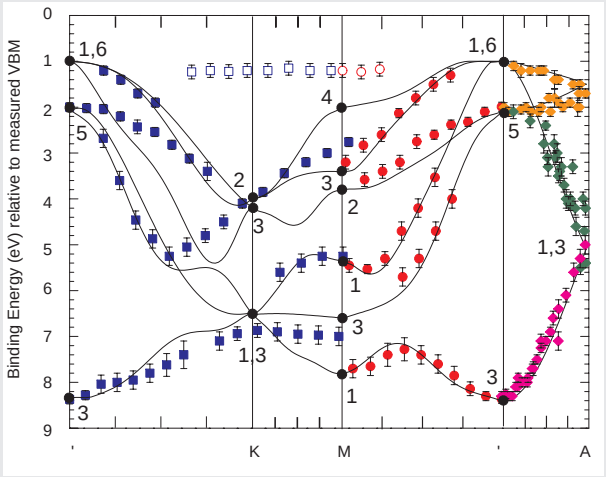

Figure M-7.

structure cannot be measured *unless* the surface is atomically clean and well-ordered.[10, 11] Achieving a reproducible method of cleaning the film surfaces was a prerequisite to all our ARP experiments. The method we used was repeated cycles of N_2 sputtering followed by annealing in UHV. Bermudez recently published an exhaustive comparison of the various methods of cleaning GaN surfaces, and found this to be one of the best approaches.[12] The spectra in **Figure M-6** and those obtained for the other high symmetry directions of the zone can be used to generate the measured bulk band structure. This is shown in **Figure M-7**, with the data points corresponding to the experimentally measured structure.[9] Also shown in **Figure M-7** as solid lines are the results of an LDA calculation by Rubio *et al.*[13] Aside from the non-dispersive state at the top of the valence band, the agreement between this calculation and the measurement is good, in terms of both variation in band width and band velocities. The non-dispersive state near the valence band maximum that we have observed can be conclusively identified as a surface state, as is discussed below.

ii) *Bulk Density of States in GaN, AlN and Related Alloys:* The last two years saw the commissioning of our new high resolution x-ray emission spectrometer on X1B. Our first experiments involved studying the bulk electronic structure of GaN thin films.[8,14] **Figure M-8a** shows both the SXE spectrum for the radiative decay of the valence band into a N *1s* hole (N *K* emission), and the SXA spectrum for excitation of N *1s* electrons into the empty conduction band (N *K* absorption). In the SXE spectrum, the N *1s* core state is excited by 430 eV photons. Details of how the emission and absorption spectra are placed on a common binding energy scale relative to the VBM can be found elsewhere.[14] The N *K* emission spectrum reflects the valence band N *2p* PDOS. **Figure M-8b** shows both the SXE spectrum for the radiative decay of the states near and in the valence band into a Ga $2p_{3/2}$ hole (Ga L_a emission), and the SXA spectrum for excitation of Ga $2p_{3/2}$ electrons into the empty conduction band (Ga *L* absorption). Here, emission from N *2p* states is dipole forbidden, and the spectrum reflects the Ga *4s* PDOS of the valence band, and the Ga *3d* shallow core state. Also shown in **Figure M-8** are the results of an LDA calculation of the PDOS for wurtzite GaN.[15] Here we have

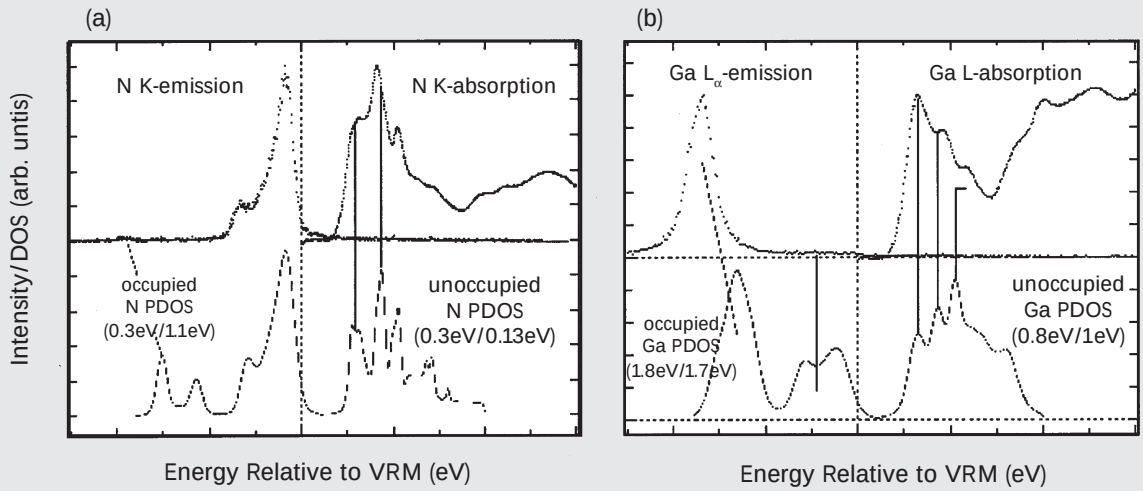

Figure M-8.

convoluted the theoretical DOS by Lorentzians to simulate the core-hole lifetime broadening and by Gaussians to simulate the instrumental broadening. The agreement between the calculated and measured PDOS for the valence and conduction bands is very good. The ability to study nitride alloy systems without worrying about cleaning their surfaces (and maintaining stoichiometry) is a particularly notable feature of SXE. Our results from the $Al_xGa_{1-x}N$ alloy system are presented in **Figure M-9**.[16,17] Here we have been able to measure the *elementally resolved* PDOS for the entire alloy system, thus allowing us to determine the evolution of the band gap as function of elemental concentration. **Figure M-9** shows the dominant N *2p* contribution to the valence band, i.e. these spectra result from the transition of N *2p* valence electrons into N *1s* holes. These spectra reveal that there is no bulk band gap bowing in this alloy system.

iii) ***Surface Electronic Structure of GaN*** : As noted earlier, there is a state visible at the top of the valence band in the experimental band structure of Figure M-7 that does not correspond to any bulk state. Using the linearly polarized nature of synchrotron radiation, we have definitively identified this state as a surface state with sp_z character. The state is destroyed by adsorption of activated H_2, and by exposure of the surface to O_2 or by ion bombardment. These measurements are performed on n-type GaN films grown by MBE. Recently, we have found that despite identical surface cleaning of the films, the electronic structure of GaN surfaces grown by MOCVD on SiC are significantly different. (Fortunately, the *bulk* states measured by ARP are the same between the MOCVD and MBE samples.) **Figure M-10** shows the experimentally measured surface band structure for MOCVD-grown GaN surfaces cleaned in *exactly* the same manner we cleaned the MBE films. For clarity, only the surface related states are plotted in **Figure M-10**, but the contrast with our results for MBE films presented in **Figure M-7** is dramatic. Instead of a spatially localized state (and hence non-dispersive in *k*-space) at the valence band maximum, we find two highly dispersive states, one of which disperses throughout almost the entire valence band. The most obvious explanation for the different results from MBE and MOCVD films whose surfaces were cleaned in the identical manner is that the surfaces

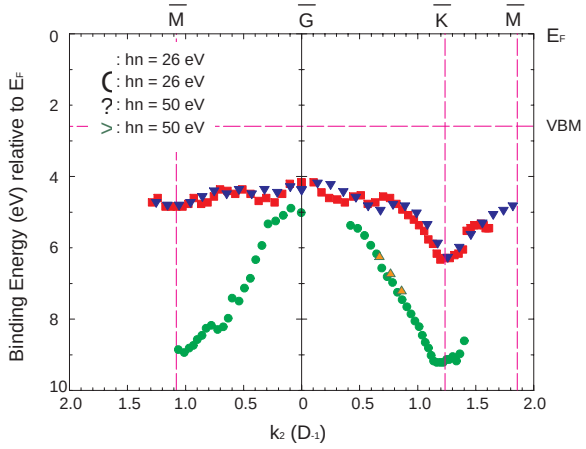

Figure M-9.

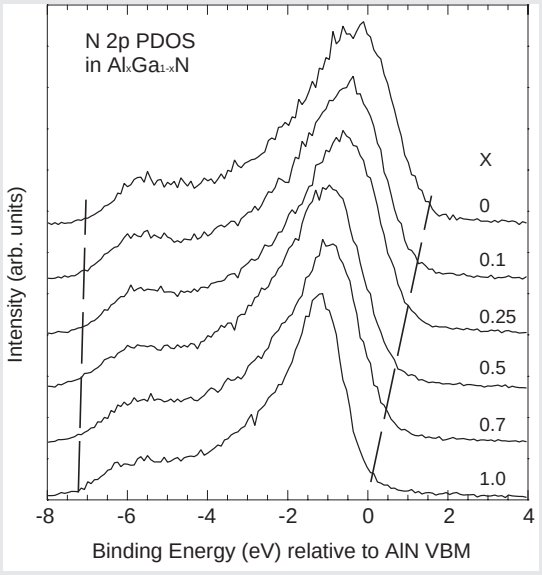

Figure M-10.

have different terminations or polarities.[9,12,18-21] Both types of surface were atomically clean (as measured using Auger electron spectroscopy) and displayed sharp (1 x 1) low energy electron diffraction (LEED) patterns indicating identical surface symmetries. However, it is likely that the termination of the surfaces is different.

iv) ***Conduction Band Dispersion in GaN*** : While soft x-ray absorption can measure the PDOS of the conduction band, inverse photoemission spectroscopy is required to measure the *dispersion* of the empty states. We began a collaboration with Peter Johnson from BNL Physics to use his high resolution inverse photoemission spectrometer.[22] Our first experiments were on MBE-grown n-type GaN. We found that there are no unoccupied surface states.[23] Furthermore, we found that the conduction band states differ significantly from free electron states up to 20 eV above E_F. Since the free electron final state assumption is used to generate the measured band structure (**Figure M-10**) from the ARP spectra, this is an important observation. However, higher photon energies were used in the band mapping, so we are satisfied the free electron final state approximation is appropriate in this case.

CONCLUSIONS

We have embarked on a multi-technique study of the electronic structure of wide band gap nitride semiconductors that employs heavily the facilities of the NSLS. This research has lead to significant progress in understanding both the surface and bulk electronic structure in simple nitrides, and in more complex alloys. Future research will be directed towards the electronic structure of overlayers and interfaces in such systems. ■

This work was performed by the Electronic Structure Group, Department of Physics, Boston University: Yu-Chang Chao, Laurent Duda, Sarnjeet Dhesi, Cristian Stagarescu, James Downes, and Philip Ryan. The inverse photoemission experiments were performed in collaboration with Tonica Valla and Peter Johnson from the Department of Physics, Brookhaven National Laboratory. Some of the SXE experiments are performed in collaboration with Jinghua Guo and Joseph Nordgren from Uppsala University. Samples are provided by Theodore Moustakas from Boston University, Robert Davis from North Carolina State University, Thorvald Anderson from Chalmers University, and Jim Edgars from Kansas State University.

Our research is supported by the NSF under DMR-9501174, and our SXE spectrometer is funded by the US ARO under DAAH04-95-0014.

REFERENCES

[1] S. Strite and H. Morkoç, *J. Vac. Sci. Technol. B* **10**, 1237 (1992).

[2] T.A. Callcott, C.H. Zhang, D.L. Ederer, D.R. Mueller, J.E. Rubensson, and E.T. Arakawa, *Nuclear Instruments and Methods* **A291**, 13 (1990).

[3] J. Nordgren, G. Bray, S. Cramm, R. Nyholm, J.-E. Rubensson, and N. Wassdahl, *Rev. Sci. Inst.* **60**, 1690 (1989).

[4] J. Nordgren and R. Nyholm, *Nucl. Inst. Methods A* **246**, 242 (1986).

[5] N.V. Smith and D.P. Woodruff, *Prog. Surf. Sci.* **21**, 295 (1986).

[6] F.J. Himpsel, *J. Phys. Chem. Solids* **49**, 3 (1988).

[7] J. Stöhr, **NEXAFS Spectroscopy** (Springer, Berlin, 1992).

[8] K.E. Smith, S.S. Dhesi, L.-C. Duda, C.B. Stagarescu, J.H. Guo, J.Nordgren, R. Singh, and T.D. Moustakas, *Mat. Res. Soc. Proc.* **449**, 787 (1997).

[9] S.S. Dhesi, C.B. Stagarescu, K.E. Smith, D. Doppalapudi, R. Singh, and T.D. Moustakas, *Phys. Rev. B* **56**, 10271 (1997).

[10] **Angle Resolved Photoemission**, edited by S.D. Kevan (Elsevier, Amsterdam, 1991).

[11] K.E. Smith and S.D. Kevan, *Prog. Solid State Chem.* **21**, 49 (1991).

[12] V.M. Bermudez, D.D. Koleske, and A.E. Wickenden, *Appl. Surf. Sci.* **126**, 69 (1998).

[13] A. Rubio, J.L. Corkill, M.L. Cohen, E.L. Shirley, and S.G. Louie, *Physical Review B* (Condensed Matter) **48**, 11810 (1993).

[14] C.B. Stagarescu, L.-C. Duda, K.E. Smith, J.H. Guo, J. Nordgren, R. Singh, and T.D. Moustakas, *Phys. Rev. B* **54**, 17335 (1996).

[15] Y.-N. Xu and W.Y. Ching, *Phys. Rev. B* **48**, 4335 (1993).

[16] L.-C. Duda, C.B. Stagarescu, J. Downes, K.E. Smith, D. Korakakis, T.D. Moustakas, J. Guo, and J. Nordgren, *Phys. Rev. B* **58**, 1928 (1998).

[17] K.E. Smith, *et al., J. Vac. Sci. Technol. B* **16**, 2250 (1998).

[18] A.R. Smith, R.M. Feenstra, D.W. Greve, M.S. Shin, M. Skowronski, J. Neugebauer, and J.E. Northrup, *Appl. Phys. Lett.* **72**, 2114 (1998).

[19] M.M. Sung, J. Ahn, V. Bykov, J.W. Rabalais, D.D. Koleske, and A.E. Wickenden, *Phys. Rev. B* **54**, 14652 (1996).

[20] A.R. Smith, R.M. Feenstra, D.W. Greve, J. Neugebauer, and J.E. Northrup, *Phys. Rev. Lett.* **79**, 3934 (1997).

[21] K. Rapcewicz, M. Buongiorno Nardelli, and J. Bernholc, *Physical Review B* (Condensed Matter) **56**, R12725 (1997).

[22] P.D. Johnson, S.L. Hulbert, R.F. Garrett, and M.R. Howells, *Review of Scientific Instruments* **57**, 1324 (1986).

[23] T. Valla, P.D. Johnson, S.S. Dhesi, K.E. Smith, T. Moustakas, and E.L. Shirley, *Phys. Rev. B* **(in press)** (1998).

X-ray Diffraction Studies on Levitated Liquids

S. Krishnan
(Containerless Research, Inc.)
S. Ansell and David L. Price
(Argonne National Laboratory)

Liquid structure measurements are important in advancing condensed matter theory, in developing predictive models, and in establishing structure-property-process relationships in high temperature materials sciences. For example, the differences between the structures of the liquid and crystalline phases of the same composition can influence the nucleation kinetics and solidification paths.

The major experimental difficulties encountered in obtaining structural data on liquids at temperatures above about 1000K are, (i) reactions of the specimens with container walls, and (ii) influence of the containers on the structural measurements. Recently, a number of research groups[1-4] have attempted to overcome these problems by employing levitation techniques in conjunction with X-ray scattering to study the structural properties of liquids. These groups have employed conical nozzle levitation (CNL)[1,2] and electromagnetic levitation techniques[3,4] to suspend 3-6 mm diameter droplets in X-ray synchrotron sources and have conducted X-ray scattering and EXAFS measurements to obtain structural data on liquids. Several key advantages of these methods include the elimination of container interactions and container-derived impurities, rapid access to high temperatures, localized heating conditions, and lastly access to the supercooled (metastable) liquid. We have used the CNL method extensively to investigate the structure of a number of liquids[5-10] in their normal and supercooled states in a series of experiments conducted at the NSLS. These prior studies include a description of the techniques[1], and structure measurements on liquid Si [5], Al_2O_3 [6], boron[7], Y_2O_3 [8], $Co_{80}Pd_{20}$ [9], Ni and Zr [10].

This article highlights a few recent results obtained on levitated liquids that were obtained with the use of conical nozzle levitation (CNL). These experiments were conducted at the X25 beamline at the National Synchrotron Light Source (NSLS) at the Brookhaven National Laboratory. The CNL apparatus consisted of a gas flow system which delivered the levitation gas (inert gases like argon) into a plenum chamber from which the gas flowed out through a divergent nozzle. Small (2-4 mm diameter) spheres of the specimen materials could be levitated stably in the nozzle. The specimens were then be laser-heated, melted and levitated for long durations of up to several hours. The complete CNL system was integrated with a with a Huber model 6-circle, X-ray diffractometer.

The CNL system was enclosed in an environmentally-controlled chamber with suitable ports for laser heating, pyrometry, sample injection and retrieval, and pressure measurements. The upper part of the chamber was a 9 inch diameter sphere. Two beryllium windows were included in this section; the first was a small window for the incident X-ray beam which was placed at the end of a radial tube port. The second window was curved and subtended approximately 120° around the nominal specimen position at the center of the chamber. This window extended about 5° below the normal levitation height of the specimen to enable transmission of the direct X-ray beam. The specimens were heated with the aid of a 270 watt CO_2 laser. Temperature measurements were obtained with two pyrometers whose operating wavelengths were 0.65 μm and 1-2.5 μm, respectively. Precise sample positioning was achieved with a 3-axis motorized translator assembly and a phosphor screen to observe the shadow of the specimen in the X-ray beam. Specimen materials could be levitated, heated, melted and positioned stably over durations of up to 3 hours, which were sufficient for the X-ray diffraction studies.

Scattered X-rays were detected using a solid-state detector with 300 eV resolution over a 2θ angular range of 10-110°. Diffraction data on liquids were obtained over a momentum transfer ($Q = 4\pi\sin(\theta)/\lambda$) range of 1.2 - 13 $Å^{-1}$. The measured intensity, $\mathbf{I(2\theta, E)}$, for an incident X-ray energy E is given by:

$$I(2\theta, E) = I_p(E)\,[A_{s,s}(2\theta, E) \bullet P(2\theta) \bullet I_{coh}(Q) + I_{MS}^{coh}]$$

$$+ I_p(E')[A_{s,s}(2\theta, E') \bullet I_{inc}(Q') + I_{MS}^{inc}(Q)] \qquad \mathbf{(1)}$$

where:

$I_p(E)$ = intensity of the main beam at the energy E,
$I_x(Q)$ = the coherent or incoherent scattering intensity,
$A_{s,s}(2\theta,E)$ = attenuation coefficient,
$I^*_{MS}(Q)$ = the coherent or incoherent multiple scattering,
$P(2\theta,E)$ = polarization factor
$E' = E + \Delta = E/(1 - 0.00392E\sin^2(\theta))$, and
$Q' = 1.014E \sin(\theta)$, where Q is measured in $Å^{-1}$ and E in keV.

This equation was used as the basis of the correction procedure which employed a Monte Carlo simulation of the experimental geometry that was then back refined against the measured data. The corrections were implemented through a two-stage refinement procedure: the first stage refined instrumental parameters, including photon density profile and detector efficiency derived from a statistical average of all the data sets obtained in the experimental run cycle, and specimen parameters including sample position in the beam, sample radius, and density. In the second stage, individual runs were analyzed using fixed instrumental and variable sample parameters. Form factors were obtained from Baro, *et al.*,[11]; the temperature dependence of the form factors was obtained from Ref. 12.

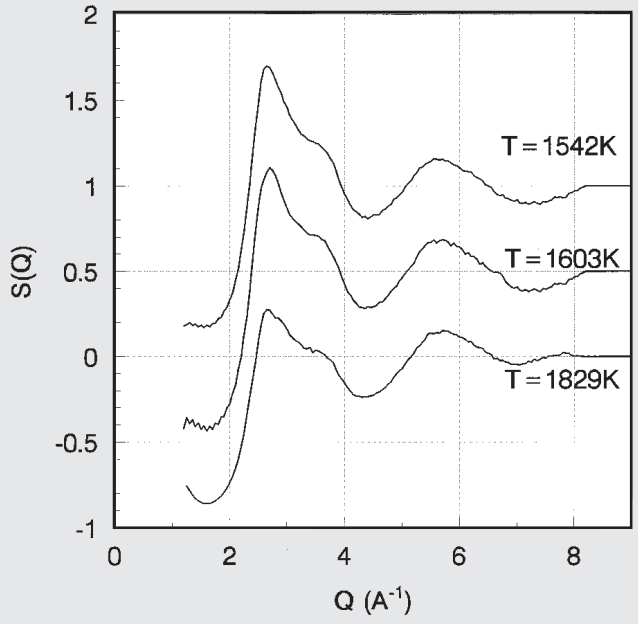

Figure M-11. Total structure factor, S(Q) for liquid Si at three specimen temperatures of 1542, 1603, and 1829K. The melting point of Si is 1688K. The S(Q) curves have been shifted for clarity.

The data analysis procedure directly yields the x-ray weighted average structure factor S(Q). From the S(Q), the radial distribution function, G(r), is given by:

$$G(r) - 1 = \frac{1}{2\pi^2 \rho_a} \int_0^{Q_{max}} Q(S(Q) - 1) \sin \frac{Qr}{r} dQ \qquad \textbf{(2)}$$

where ρ_a is the number of atoms per unit volume. This inverse Fourier transform method employs the maximum entropy criterion [13] where G(r) is constrained to one at large r. Values of the number density, ρ_a, was either estimated or obtained from literature data.

In this article, we will present structural results (obtained at the X25 beamline) on liquid silicon[5] and boron[7] in the normal and supercooled liquid states. **Figure M-11** shows the X-ray weighted average structure factors S(Q) for liquid Si at temperatures of 1542, 1603, and 1829K. The melting point of Si is 1688K, so that the first and second measurements correspond to the supercooled liquid state. The S(Q) shows a main peak with a pronounced shoulder on the high-Q side in addition to a second peak. Figure **M-12 (Table)** lists the locations of the peaks in the S(Q) for liquid Si. The significant effect of supercooling is to move the first peak and shoulder to a Q value that is about 8% greater at 1542K than at 1829K. Pair correlations functions g(r) were obtained from the S(Q) using a maximum entropy method[13] and are given in **Figure M-13**. Supercooling results in a significant sharpening of the first peak and a reduction in the coordination number from 6.4 to 5.6. A systematic decrease of 2% in the position of the first peak is observed with supercooling, as given in **Figure M-12**. The stable liquid shows a shoulder on the high-r side of the first peak, which splits into a double shoulder upon supercooling. The present results for liquid Si above the melting point were found to be in good agreement with the prior measurements of Waseda, *et al.*[14] and in fair agreement with the *ab initio* MD simulations of Stich, *et al.*[15]. The decrease in the first peak maximum and the first shell coordination with supercooling is consistent with the MD simulations of Angell and Borick[16]. Further discussion of the structural measurements and a discussion of results obtained on liquid Si results can be found in a recent publication[5].

Figure M-12 (Table). Structural results for liquid Si and B; S(Q), g(r), and coordination (C_n)

		S(Q)			g(r)				
	Temp	Q_1	hump	Q_2	r_1	sub1	sub2	r_2	C_n
	(K)	Å^{-1} ±0.03	Å^{-1}	Å^{-1} ±0.03	Å ±0.03	Å ±0.03	Å	Å ±0.05	atoms ±0.5
Silicon (m.p 1688K)									
Si	1542	2.65	3.65	5.65	2.41	3.28	3.98	5.22	5.6
Si	1603	2.70	3.60	5.70	2.42	3.27	3.95	5.22	5.6
Si	1829	2.45	3.55	5.45	2.46	3.45		5.20	6.4
Si [15]	1800	2.63	3.55	5.68	2.46	3.64		5.64	6.2
Boron (m.p. 2360K)									
B	2600	2.50		4.40	1.76			3.15	5.8
B	2400	2.50		4.45	1.78			3.16	5.8
B	2090	2.45		4.35	1.78			3.15	6.2
B [17]					1.71			3.18	6.0

The crystalline forms of boron embody some of the most complex crystal structures for a pure element. The α-rhombohedral, β-rhombohedral and tetragonal crystalline forms have a very large number of atoms per unit cell, and are dominated by the B_{12} icosahedron structural unit. Based on surface tension, entropy of melting and stability data, it was speculated that these icosahedrons may survive upon melting. Because of the very high reactivity of boron at high temperature, the liquid phase had never been studied prior to the present work which employed levitation to access the liquid phase. **Figure M-14** shows the pair correlation function, g(r), for liquid boron at temperatures of 2600, 2400, and 2090K [7]. The melting point of boron is 2360K. The positions of the peaks in the g(r) are not significantly affected by temperature, although there is a sharpening of the second and third peaks upon supercooling and an increase in the first shell coordination (**Figure M-12**). The liquid g(r) compares well with those predicted in a recent *ab initio* MD study[17]. The liquid g(r) is also similar to the g(r) for the different crystalline forms, but the absence of a low Q peak near 1 Å^{-1} in the S(Q) [see ref. 7] does not provide conclusive proof of the existence of B_{12} icosahedral units. Nevertheless, the first direct measurement of the structure of liquid B shows that the short-range structure is remarkably similar to the crystalline and amorphous solid forms, with little change in bond lengths but a broadening of the first coordination shell, preserving the coordination number around a value of 6. The present study shows that boron is unique among covalently-bonded solids in undergoing an insulator to metal transition on melting with small volume expansion and little change in the short-range structure. ■

This work was supported by the US Department of Energy SBIR Contract number DE-FG02-94ER81732 and by Division of Materials Sciences, Office of Basic Energy Sciences, under Contract W-31-109-ENG-38. The authors thank Dr. Lonny Berman of NSLS for his help with the experiments. The National Synchrotron Light Source at Brookhaven National Laboratory is supported by the Division of Materials Sciences and Chemical Sciences of the DOE.

REFERENCES

[1] S. Krishnan, J. J. Felten, J. E. Rix, J. K. R. Weber, P. C. Nordine, S. Ansell, M. A. Beno, and D. L. Price, *Rev. Sci. Instrum.*, **68**, 3512 (1997).

[2] C. Landron, X. Launay, J. C. Rifflet, P. Echegut, Y. Auger, D. Ruffier, J. P. Coutures, M. Lemonier, M. Gailhanou, M. Bessiere, D. Bazin, H. Dexpert, *Nuclear Instruments and Methods in Physics Research B.,* **124**, 627 (1997).

[3] G. Jacobs, I. Egry, K. Maier, D. Platzek, J. Reske, and R. Frahm, *Rev. Sci. Instrum.,* **67**, 3683 (1996).

[4] D. Herlach, Private Communication, 1998.

[5] S. Ansell, S. Krishnan, J. J. Felten, and D. L. Price, *J. Phys. Cond. Matt.*, **10**, L73(1998).

[6] S. Ansell, S. Krishnan, J. K. R. Weber, J. J. Felten, P. C. Nordine, M. A. Beno, M-L. Saboungi, and D. L. Price, *Phys. Rev. Lett*, **78**, 464 (1997).

[7] S. Krishnan, S. Ansell, J. J. Felten, K. J. Volin, and D. L. Price, *Phys. Rev. Lett.*, **81** 576 (1998).

[8] S. Krishnan, S. Ansell, and D. L. Price, *J. Am. Ceram. Soc.*, **81 (7)**, 1967 (1998).

[9] S. Krishnan, S. Ansell, and D. L. Price, in Press, Proc. of the Tenth International Conference on Liquid and Amorphous Metals, Dortmund, Germany, 1998.

[10] S. Ansell, S. Krishnan and D. L. Price, Submitted for publication to *Phys. Rev. Lett.*

[11] J. Baro, M. Roteta, J. M. Fernandez-Varea, and F. Salvat, *Radiat. Phys. Chem.*, **44**, 531 (1994).

[12] J. Chihara, *J. Phys. F: Met. Phys.*, **17**, 295 (1987).

[13] A. K. Soper, *Inst. Phys. Conf. Proc. R. Soc.*, **97**, 711 (1989).

[14] Y. Waseda, K. Shinoda, K. Sugiyama, and S. Takeda, *Jpn. J. Appl. Phys.*, **34**, 4124 (1995).

[15] I. Stich, R. Car, and M. Parrinello, *Phys. Rev. Lett.,* **63**, 2240 (1989).

[16] C. A. Angell and S. Borick, Submitted for publication to *J. Phys. Cond. Matt.*, 1998.

[17] N. Vast, S. Bernard, and G. Zerah, *Phys. Rev. B.*, **52**, 4123 (1995).

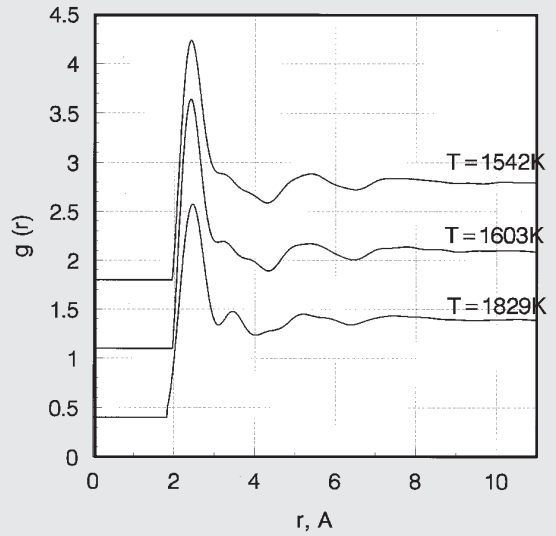

Figure M-13. Radial distribution function, g(r) for liquid Si at three specimen temperatures of 1542, 1603, and 1829K computed using the maximum-entropy Fourier transform method. The melting point of Si is 1688K. The g(r) curves have been shifted for clarity.

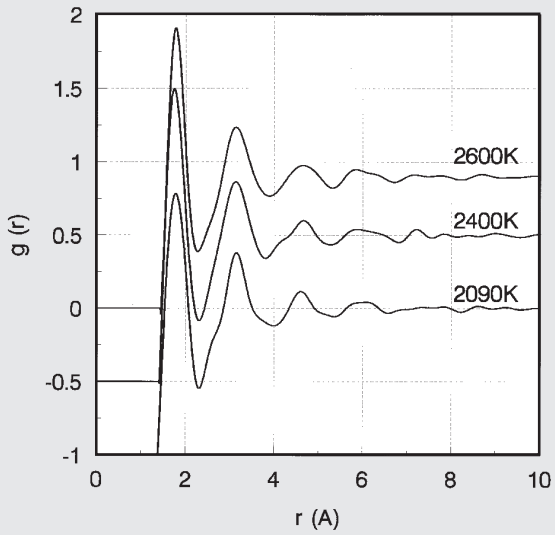

Figure M-14. Radial distribution function, g(r) for liquid B at three specimen temperatures of 2600, 2400, and 2090K computed using the maximum-entropy Fourier transform method. The melting point of B is 2360K. The g(r) curves have been shifted for clarity.

Direct Observation of Charge and Orbital Ordering in Manganites

M. v. Zimmermann, J.P. Hill, Doon Gibbs, M. Blume (BNL Physics Dept.)
Y. Murakami (Photon Factory, Japan)
Y. Tomioka (Joint Research Center for Atom Technology (JRCAT), Japan)
Y. Tokura (University of Tokyo, Japan)

Understanding the origins of high-T_c superconductivity and colossal magnetoresistence are among the most intensely studied issues of physics research today. Intriguingly, both phenomena appear in perovskite-type transition metal oxides, which share the common characteristic that the electrons are neither localized nor completely delocalized, but behave in an intermediate fashion. These materials are known as strongly correlated electron systems and it is believed that their unusual properties result from these correlations.

The doped manganites are one class of materials where such behavior can be investigated. The manganites are fundamentally interesting because the four main characteristics of strongly correlated systems, the spin, charge, orbital and lattice degrees of freedom, are all present. In addition, members of this class exhibit colossal magnetoresistance phenomena, in which the measured magnetoresistance can change by 6-8 orders of magnitude in an applied magnetic field. This has attracted considerable attention because of possible applications in the magnetic recording industry and elsewhere.

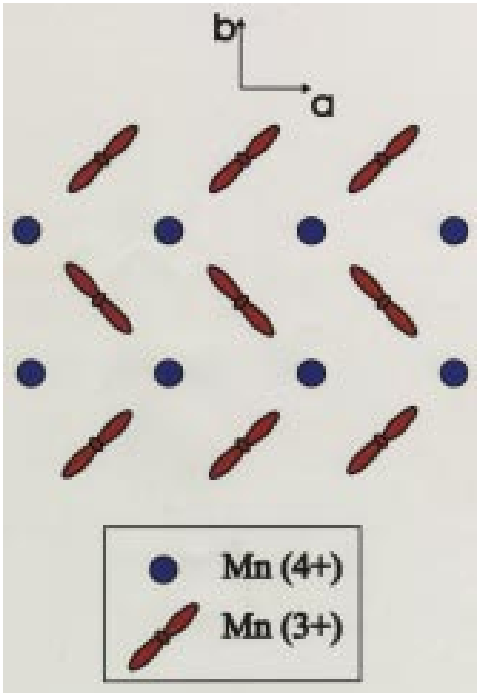

Figure M-15. Pattern of charge and orbital ordering in $Pr_{0.6}Ca_{0.4}MnO_3$.

Here, we briefly report our results on $Pr_{1-x}Ca_xMnO_3$ for x=0.4, and illustrate the use of resonant x-ray scattering techniques to probe the orbital and charge degrees of freedom directly. This is a new development in the field which holds enormous promise for helping to understand the unusual behavior exhibited by manganites. For $Pr_{0.6}Ca_{0.4}MnO_3$ the spin ordering occurs at 170 K, while the charge and orbital ordering occurs at a significantly higher temperature of about 240 K. In these experiments, we have been able to observe critical fluctuations of both the orbital and charge order at temperatures above the phase transition. We have discovered that, while the two order parameters have the same temperature dependence below the phase transition, they exhibit very different behaviors above. Specifically, the charge order fluctuations have a longer length scale than the orbital order fluctuations, for a given temperature. This in turn suggests that it is the charge order that is driving this phase transition, which is an important insight.

The charge ordering The charge ordering in these systems manifests itself in an alternating pattern of Mn^{3+}/ Mn^{4+} valences as shown in **Figure M-15**. Associated with this ordering pattern is a lattice distortion which has been studied in detail in related systems by neutron and electron diffraction[1]. Direct information concerned with the valence of the Mn-atoms is gained by resonant X-ray diffraction via the anomalous dispersion of the Mn^{3+} and Mn^{4+} scattering factors. The slight difference in the Mn^{3+} and Mn^{4+} absorption energies leads to an anomaly in the scattered peak intensity at the charge order superlattice peak when the incident photon energy is tuned to the manganese K absorption edge[2].

Orbital ordering in these systems refers to the long ranged orientation of the occupied Mn 3d orbitals in a periodic pattern. In a first approximation, the electronic configuration of Mn^{3+} in this compound is (t_{2g}^3, e_g^1). The t_{2g}-electrons are localized, while the e_g-electrons are more

delocalized, and they occupy either $(3z^2\text{-}r^2)$ or $(x^2\text{-}y^2)$-type orbitals. It is the e_g orbitals, present only on the Mn^{3+} ions, which order periodically (**Figure M-15**). Very recently, it has been demonstrated that it is possible to probe this ordering of the orbitals by means of resonant X-ray scattering[2, 3]. The asphericity of the atomic electron density leads to the observation of forbidden reflections and a dramatic enhancement of the scattered intensity results when the incident photon energy is tuned to the Mn-resonance energy. Two characteristics of the orbital ordering superstructure reflection are that the polarization of the incident beam is rotated from σ to π and that the intensity depends on the azimuthal angle according to $I(\phi) \propto \sin^2(\phi)$. This latter behavior is in distinct contrast to the azimuthal dependence of a regular Bragg peak, which is independent of ϕ. These features of the scattering allow one to identify peaks arising from orbital order unambiguously[2, 3].

One of the most fascinating issues to be probed concerns the interaction between the charge and orbital ordering. In particular, it is not clear whether the two sublattices order independently, or if one drives the other. We have investigated the critical temperature range of the charge and orbitally ordered regime by means of resonant x-ray scattering, in order to gain insight into this question.

The experiments were performed at beamline X22C at the National Synchrotron Light Source. The beamline is equipped with a focusing toroidal mirror and a Ge(111) double monochromator with an energy resolution of about 5 eV. The polarization of the scattered beam was analyzed with a Cu(220) analyzer crystal. A single crystal of $Pr_{0.6}Ca_{0.4}MnO_3$ was cooled with a standard displex refrigerator.

Because the charge and orbital order have different periodicity, they give rise to superlattice peaks at different positions in reciprocal space, and the two types of order may be studied independently. The charge ordering was measured in a σ-σ scattering geometry at the (0 3 0) superstructure reflection and the orbital order at the (0 2.5 0) superstructure reflection in a σ-π geometry. In this notation the fundamental Bragg reflections occur at (0 2n 0), where n is an integer. **Figure M-16** shows the peak intensities and full width at half maximum of the charge and orbital ordering plotted versus temperature. The intensities show a sharp drop at T=240 K for both the charge- and the orbital ordering peaks, consistent with a first order transition. A few degrees above the transition temperature, fluctuations are observed at both the charge and orbital order positions. Remarkably, as seen from the peak width, shown in the bottom part of **Figure M-16**, the inverse correlation length for the orbitally ordered phase increases significantly faster with increasing

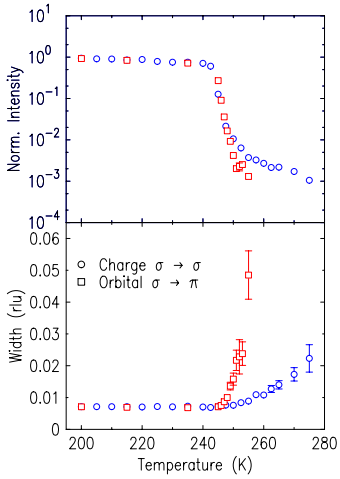

Figure M-16. Comparison of the peak intensity (top) and the peak width (bottom) of the charge peak (0 3 0) (blue circles) measured in a σ-σ geometry and the orbital order peak (0 2.5 0) (red squares) measured in a σ-π geometry.

temperature than that of the charge order. This behavior indicates that the charge order is better established at a given temperature than the orbital order, suggesting that a charge ordered phase is a prerequisite for orbital ordering. In particular, these results imply that it is the charge order which drives the phase transition. While more detailed investigations are still required, these results %extremely interesting and beautifully demonstrate the power of this new technique for the study of charge and orbital degrees of freedom, opening a new window on these intriguing and complex systems.■

REFERENCES

[1] E.O. Wollan and W.C. Koehler, *Phys. Rev.* **100**, 545, (1955).

[2] Y. Murakami, H. Kawada, H. Kawata, M. Tanaka, T. Arima, Y. Morimoto and Y. Tokura, *Phys. Rev. Lett.* **80**, 1932, (1998).

[3] Y. Murakami, J.P. Hill, Doon Gibbs, M. Blume, I. Koyama, M. Tanaka, H. Kawata, T . Arima, Y. Tokura, K. Hirota and Y. Endoh, *Phys. Rev. Lett.* **81**, 582, (1998).